

# Monocular Fisheye Camera Depth Estimation Using Semi-supervised Sparse Velodyne Data

Varun Ravi Kumar<sup>†</sup>, Stefan Milz<sup>†</sup>, Martin Simon<sup>†</sup>, Christian Witt<sup>†</sup>,  
Karl Amende<sup>†</sup>, Johannes Petzold<sup>†</sup>, Senthil Yogamani<sup>\*</sup>

Valeo Schalter und Sensoren GmbH<sup>†</sup>, Valeo Vision Systems<sup>\*</sup>

{varun-ravi.kumar, stefan.milz, martin.simon, christian.witt}@valeo.com  
{karl.amende, johannes.petzold, senthil.yogamani}@valeo.com

**Abstract.** Near-field depth estimation around a self-driving car is an important function that can be achieved by four wide-angle fisheye cameras having a field of view of over  $180^\circ$ . CNN based depth estimation produce state of the art results, but progress is hindered because depth annotation cannot be obtained manually. Synthetic datasets are commonly used but they have limitations. For instance, they do not capture the extensive variability in the appearance of objects like vehicles present in real datasets. There is also a domain shift while performing inference on natural images illustrated by many attempts to handle the domain adaptation explicitly. In this work, we explore an alternate approach of training using sparse LIDAR data as ground truth for depth estimation for fisheye camera. We built our own dataset using our self-driving car setup which has a 64-beam Velodyne LIDAR and four wide angle fisheye cameras. LIDAR data projected onto the image plane is sparse and hence viewed as semi-supervision for dense depth estimation. To handle the difference in view-points of LIDAR and fish-eye camera, an occlusion resolution mechanism was implemented. We started with Eigen’s multiscale convolutional network architecture [1] and improved by modifying activation function and optimizer. We obtained promising results on our dataset with RMSE errors better than the state-of-the-art results obtained on KITTI because of vast amounts of training data. Our model runs at 20 fps on an embedded platform Nvidia TX2.

## 1 Introduction

Depth estimation from single camera images is an important basic task for self driving cars such as driver assistance systems to solve localization and perception problems. Predominantly, the challenge is an arduous process and it cannot be decoded directly from bottom-up geometric cues. A single captured image scene may be congruous with infinite real world scenarios [2]. Successful approaches have relied on structure from motion, shape-from-X, binocular and multi-view stereo. These techniques hinge on the assumption of prior knowledge about the characteristic appearance and multiple observations of the scene of interest that are available. The aforementioned can occur via multiple viewpoints, layout and size of object needs, cues such as shading, or observations of the scene under different lighting conditions. To overcome this limitation, there has recently been a rise in the number of works that pose the task of single image depth estimation as a supervised learning problem [1,2,3]. These methods seek to

directly predict the depth of each pixel in an image through deep learning models that have been modeled on large collections of ground truth depth data.

A large amount of training data is required for supervised deep learning in order to achieve high accuracy and to generalize on new scenes. Depth sensors are typically used to capture ground truth. In indoor environment, RGB-D cameras are usually used. The usage of RGB-D cameras in the domain of self driving cars will limit the field of view [4]. Outdoor applications currently bank on LIDAR or other laser scanners-an integral component for the self driving cars. There are many shortcomings using such sensing devices.

Firstly, strong sunlight can have an adverse effect on infrared interference and make depth information extremely noisy, which will be learned by the network. Due to these obstacles, it has paved the way for wide research interest in estimating depths from single RGB images [3]. It is found that the measurements from 3D lasers are usually much sparser than the images and identification of high-detail depth variations - visible in the image - is less successful. Finally, precise extrinsic and intrinsic calibration of the sensors are required. In addition to this, synthetic rendering of depth maps is used to generate ground truth data. Rendered images do not unveil the scene and fail to implement real image noise characteristics-which are the two drawbacks of this method [5]. Also, there is an inefficiency to generalize on new scenes by the model trained on this approach.

Humans excel at monocular depth estimation by exploiting cues such as motion parallax, linear perspective, shape from shading, relative size and occlusion [6]. Full scene understanding with our capability to precisely estimate depth appears to bolster from the combination of both top-down and bottom-up cues [7].

For monocular depth estimation, we adopt the approach of Eigen et al. [1,2] trained on images and their corresponding depth values -where the first network estimates the global structure of the scene and second that refines it using local information. The same loss function is used to train the network that explicitly accounts for depth relations between pixel locations, in addition to point wise error. Eigen's approach does not rely on handcrafted features or an initial over-segmentation as compared to earlier approaches in single image depth estimation. Instead, they cultivate a representation directly from the raw pixel values. Relying on the achieved estimation rates on the KITTI [4] and on improved qualitative output, the approach was tested on our internal, extremely sparse, occlusion removed dataset. We could achieve similar qualitative output on our sparse LIDAR data and fisheye camera images.

The motivation of this paper is to provide a baseline for single frame depth estimation based on sparse Velodyne data as ground truth for training. Velodyne data re-projected to image plane is very sparse and is a form of semi-supervision for learning dense depth. Contributions of this paper include:

1. Demonstration of a working prototype purely trained on semi-supervised Velodyne LIDAR data.
2. Demonstration of fisheye camera depth estimation using CNN.
3. Adapting training data to handle occlusion due to difference in camera and Velodyne LIDAR viewpoint.
4. Tailoring the loss function and training algorithm to handle semi-supervision.

The rest of the paper is structured as follows. Section 2 provides a survey of convolution neural networks (CNN) based depth estimation. Section 3 discusses the details of the network architecture, loss function tailoring and training algorithms. Section 4 summarizes results on our internal fisheye camera dataset and provide a comparison with publicly available KITTI results. Finally, Section 5 concludes the paper and provides potential future directions.

## 2 Related Work

It has been noted that in recent years, several deep learning based approaches to monocular depth estimation are trained in a supervised way - which requires a single input image - with no assumptions about the scene geometry or types of objects which are present. In monocular depth estimation only single image is used at the inference time. Saxena et al. [8] pioneered the supervised-learning based approach called Make3D patch-based model. The input images are initially over-segmented into patches and the 3D location and orientation of local planes are estimated which illustrates each patch. Dataset from laser scans are used to train a linear model to obtain the estimates of the plane parameters. Markov Random Fields are used to combine the monocular cues with the stereo correspondences. The drawback of planar based approximations including [9] is realistic outputs can not be generated as they lack global context since the estimates are made locally. They can be hindered when it comes to modeling of thin structures.

Liu et al. [3] formulated an approach for depth estimation as a deep continuous Conditional Random Fields (CRF) learning problem. Instead of hand-raffing features such as unary and pairwise terms, Liu used deep convolutional neural fields that permitted the CNN features of unary and pairwise potentials end-to-end for training by utilizing continuous depth and Gaussian assumptions on the pairwise potentials.

Ladicky et al. [10] improved the per pixel depth estimation to a lucid classifier estimating only the probability of a pixel present at an arbitrarily fixed canonical depth. After appropriate image transformations, the probability of any other depths can be achieved by implementing the same classifier. The vulnerability of independent approaches of depth estimation and semantic segmentation are aimed directly by improving and generalizing the overall approach.

Karsch et al. [11] recommended a k-Nearest-Neighbor (kNN) transfer mechanism which can achieve better alignment which hinges on SIFT Flow [12] to estimate depths from single images of static backgrounds. They accomplished better estimation with the scene of interest in videos with dynamic foreground coupled with augmentation of the latter with motion information. A major drawback of this approach is a requirement of a complete training dataset to be available at inference time.

In the last few years, it has been observed that object classification and recognition [13,14,15,16,17] reap great success with the application of Convolutional Neural Networks. CNNs perform classification of a single or multiple object label for a complete input image and apply bounding boxes on a few objects in each scene of an image. In addition to this, a variety of tasks like pose estimation [18,19], stereo depth [20,21] and instance segmentation [22] incorporate CNNs. Most of these models use CNNs to

find only local features, or generate descriptors of discrete proposal regions; in contrast, Eigen’s network uses both local and global views to predict a variety of output types.

Laina [23] illustrated that dense depth maps can be produced by using ResNet-based encoder-decoder architecture. Their approach is demonstrated to predict dense depth maps in indoor scenes using RGB-images for training. Through example images [24,25,26] it is found that the idea of depth transfer can be used to predict depth map or integrate depth map prediction with semantic segmentation [1,10,27,28,29] in supervised training.

Single-image based depth estimation has various hardware-based solutions like performing depth from defocus using a modified camera aperture proposed by Levin et al. [30] and the Kinect v2 uses time-of-flight and active stereo to record depth. These kind of sensors (Kinect and Kinect v2) are used indirectly by Eigen et al. [2] which provides ground truth depth targets for training the model. Although, the system is entirely software-based during inference time, predicting depth from RGB images.

We have incorporated Eigen’s [1] core multi-scale architecture to adapt to a single task of estimating depth with an output resolution twice the original. We could achieve similar qualitative results with a sparse dataset, obtained from Velodyne HDL-64L rotating 3D laser scanner with valid depth points ranging from 3k-25k after occlusion removal.

### 3 Model Architecture & Training Algorithm

Our model offers several architectural improvements to [1] which is initially based on Eigen et al. [2]. We adopted a simple architecture for Scale 1 based on AlexNet [13] to achieve real time on an embedded platform Nvidia TX. However, the usage of new model architectures such as ResNet-50 [31] which have a bigger field of view could improve the results. These models take images of bigger dimensions as input and hence can provide a better global view of the image to the learning algorithm. Depending on the whole image area, a multi-scale deep neural network first predicts a coarse global output and refines it using finer-scale local networks. This scheme is described in Fig. 1. The model is deeper with more convolutional layers compared to [2]. Second, with the added third scale from [1] at higher resolution, bringing the final output resolution up to half the input, or  $284 \text{ px} \times 80 \text{ px}$  for our sparse LIDAR fisheye camera dataset. In addition, we use swish [32] as the activation function rather than the mostly preferred ReLU [33]. Finally, we adopt Adam optimizer [34] which yields better training error/loss instead of the Stochastic gradient descent (SGD) used by Eigen et al. [1,2]. Multi channel feature maps were passed similarly to [1] avoiding the flow of output predictions from the coarse scale to the refine scale.

**Scale 1: Full-Image View** The first scale of the neural network analyses the global structure of the image and extracts global features. Global understanding of the scene requires an effective use of depth cues like object locations, vanishing points and alignment of structures [1]. The local view of the image is inadequate to capture these features. Scale 1 is based on an ImageNet-trained AlexNet [13] with initialization of pre-trained AlexNet weights only on convolutional layers. The global understanding of the

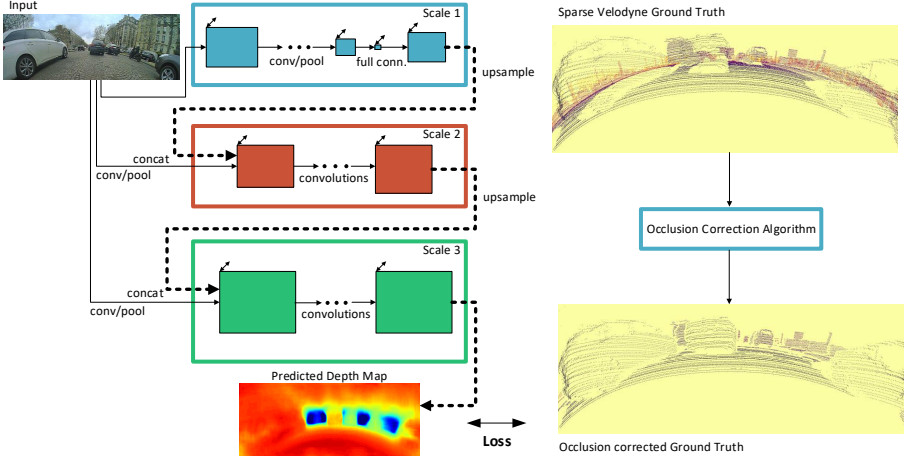


**Fig. 1.** Multi-scale architecture for depth prediction on raw fisheye images with a sparse velodyne (HD64L) ground truth. Occlusion correction is essential, if velodyne points are mapped to the fisheye eye image plane, because of the different mounting positions of camera and LIDAR (see Section 3.4).

image is achieved by two fully connected layers at the end. A very large field of view is obtained as each spatial location in the output connects to all the image features. The neural network takes fisheye images of size  $576 \text{ px} \times 172 \text{ px}$  as input. The output of the scale is a 64-channel feature map with a resolution  $142 \text{ px} \times 40 \text{ px}$ .

**Table 1.** Scale 1 (Alex Net) of the Multi-Scale Convolutional Neural Network

	Conv1	Pool1	Conv2	Pool2	Conv3	Conv4	Conv5
<b>Resolution</b>	$142 \times 41$	$71 \times 21$	$71 \times 21$	$36 \times 11$	$36 \times 11$	$36 \times 11$	$36 \times 11$
<b>Channels</b>	96	-	256	-	384	384	256
<b>Kernel Size</b>	$11 \times 11$	$3 \times 3$	$5 \times 5$	$3 \times 3$	$3 \times 3$	$3 \times 3$	$3 \times 3$
<b>Stride</b>	4	2	1	2	1	1	1
	Pool5	FC6	FC7	Reshape	Upsample	Slice	
<b>Resolution</b>	$18 \times 6$	$1 \times 1$	$1 \times 1$	$36 \times 10$	$144 \times 40$	$142 \times 40$	
<b>Channels</b>	-	4096	23040	64	64	64	
<b>Kernel Size</b>	$3 \times 3$	-	-	-	-		
<b>Stride</b>	2	-	-	-	-		

**Scale 2: Predictions** This scale incorporates a narrow view of the image and makes depth predictions at a resolution one-fourth of the input image [1] as shown in Table 2. While making predictions, the global scene information supplied by the Scale 1 is also

**Table 2.** Scale 2 of the Multi-Scale Convolutional Neural Network

	Conv1	Pool1	Slice	Concat	Conv2	Conv3
<b>Resolution</b>	$284 \times 82$	$142 \times 41$	$142 \times 40$	$142 \times 40$	$142 \times 40$	$142 \times 40$
<b>Channels</b>	96	-	-	160	64	64
<b>Kernel Size</b>	$9 \times 9$	$3 \times 3$	-	-	$5 \times 5$	$5 \times 5$
<b>Stride</b>	2	2	-	-	1	1
	Conv4	Conv5	Upsample			
<b>Resolution</b>	$142 \times 40$	$142 \times 40$	$284 \times 80$			
<b>Channels</b>	64	1	1			
<b>Kernel Size</b>	$5 \times 5$	$5 \times 5$	-			
<b>Stride</b>	1	1	-			

considered by concatenation of feature maps. The input to this scale is the same RGB image which was given as input to Scale 1. Similar to the first scale, the input image has been resized to  $576 \text{ px} \times 172 \text{ px}$ . Scale 2 corrects the coarse prediction it receives from Scale 1 to align with local details such as object and car edges, by concatenating the feature maps of the coarse network with those from a single layer of convolution and pooling. The output of the second scale is a  $284 \text{ px} \times 80 \text{ px}$  prediction for our sparse fisheye cameras dataset, with a single channel as a gray scale image.

**Scale 3: Higher Resolution** Scale 3 represents the final scale of the architecture as shown in Table 3. This scale refines the predictions made by Scale 2. It contains a set of convolutional operations with a small stride that can blend detailed structure of the image into the predictions. The alignment of output to higher-resolution details is further refined which produces detailed spatially coherent depth map predictions. The final linear layer of this scale predicts the depth map with a resolution of  $284 \text{ px} \times 80 \text{ px}$ .

**Table 3.** Scale 3 of the Multi-Scale Convolutional Neural Network

	Conv1	Pool1	Slice	Concat	Conv2	Conv3	Conv4
<b>Resolution</b>	$284 \times 82$	$284 \times 82$	$284 \times 80$	$284 \times 80$	$284 \times 80$	$284 \times 80$	$284 \times 80$
<b>Channels</b>	63	-	-	64	64	64	1
<b>Kernel Size</b>	$9 \times 9$	$3 \times 3$	-	-	$5 \times 5$	$5 \times 5$	$5 \times 5$
<b>Stride</b>	2	1	-	-	1	1	1

### 3.1 Sparse ground-truth depth maps

The Velodyne LIDAR HDL-64ES2 sensor can fire only 64 beams of lasers at different vertical angles with a vertical field of view of  $26.8^\circ$ . Hence the depth maps obtained

from the projection of the LIDAR 3D points are sparse. Due to rotary motion of the Velodyne LIDAR sensor and movement of the vehicle while data recording was made, points that are far away had poor reflectivity. Therefore the extracted depth maps are sparser for scenes composed of far away objects.

The resolution of depth maps obtained after projection of 3D LIDAR points is  $1280 \text{ px} \times 800 \text{ px}$  pixels and this corresponds to our active array size of the fisheye cameras. To have a good field of view of the scene and to preserve the aspect ratio considering the nature of the neural network, depth maps and fisheye camera RGB images are cropped. Cropping is done in the area that has maximum concentration of valid pixels. Dimensions of the images after cropping is  $1100 \text{ px} \times 330 \text{ px}$ . Also cropping is essential to remove the obstruction in the field of view caused by the mounting positions of the fisheye cameras.

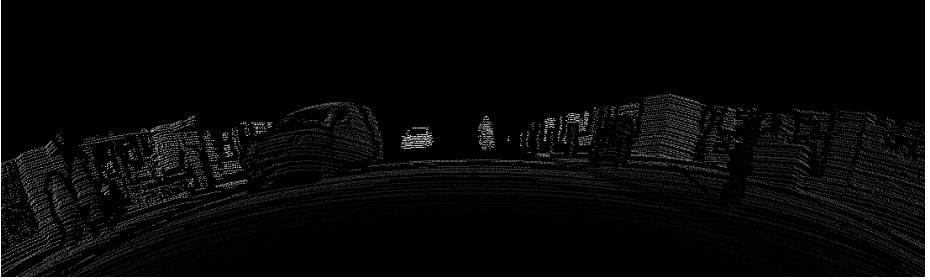


**Fig. 2.** An example of sparse Velodyne LIDAR ground truth generated depth map.

The sparse nature of the ground truth depth maps is considered in the design of the loss function as explained in Section 3.2.

### 3.2 Scale-Invariant Error

We have adopted the same loss function as described by Eigen et al. [2] which is a  $l_2$ -loss with a scale-invariant term. There is a lot of uncertainty regarding the scale associated with the image, since we consider only a single image for depth prediction. Several outdoor traffic scenes could produce the same depth map differing only by the scaling factor. The intuition behind this is the fact that the same object differing only by size could have similar depth map differing only by some scaling factor, if captured from different distances. The scale-invariant loss considers this scaling effect and produces the same loss for two outdoor traffic scenes that differ only by the scaling factor. Last linear layer in the third scale of the architecture predicts the depth, which is compared to the ground truth depth map. The loss function is defined by equation 4, where  $p$  is the pixel wise set of predictions from the neural network.  $p^*$  represents the ground truth depth map. Hence,  $d_i = p_i - p_i^*$  is the difference for pixel  $i$ . The ground truth depth map is sparse, i.e. not for all pixels exists an equivalent depth measurement. We define a set of valid pixels  $V \subset P^*$ , with  $V = \{p_1 \dots p_i \dots p_n\}$ , where  $n$  is the number of valid pixels within the ground truth depth map [2]:

$$\text{Loss}(p, p^*) = \frac{1}{n} \sum_{i \in V} (\log p_i - \log p_i^* + \alpha(p, p^*))^2. \quad (1)$$

For a given  $(p, p^*)$ , the error is minimized by  $\alpha$ . The value of  $\alpha$  is  $\alpha(p, p^*) = \frac{1}{n} \sum_{i \in V} (\log p_i^* - \log p_i)$ . The scale that best aligns to the ground truth is given by  $e^\alpha$  for any prediction  $p$ . The error is same across all the scalar multiples of  $p$ , hence the term scale invariance as mentioned in [2].

An equivalent form of metric was obtained by Eigen et al. [2] by setting  $d_i = \log p_i - \log p_i^*$  to be the difference between the prediction and ground truth at pixel  $i$ ,

$$\text{Loss}(p, p^*) = \frac{1}{n^2} \sum_{i, j \in V} ((\log p_i - \log p_j) - (\log p_i^* - \log p_j^*))^2 \quad (2)$$

$$\text{Loss}(p, p^*) = \frac{1}{n} \sum_{i \in V} d_i^2 - \frac{1}{n^2} \sum_{i, j \in V} d_i \cdot d_j \quad (3)$$

$$\text{Loss}(p, p^*) = \frac{1}{n} \sum_{i \in V} d_i^2 - \frac{1}{n^2} \left( \sum_{i \in V} d_i \right)^2 \quad (4)$$

The error is demonstrated in equation 2 by comparing the relationships between pairs of pixels  $i, j$  in the output: each pair of pixels in the prediction must differ in depth by an amount similar to that of the corresponding pair in the ground truth to have a low error.

The metric to the original  $l_2$  error is related by Equation 3, but with an additional term,  $-\frac{1}{n^2} \sum_{i, j} d_i \cdot d_j$ , mistakes are credited if they are in the same direction and penalized if they oppose. Therefore, when the mistakes are consistent with one another, an imperfect prediction will have a low error. Equation 4 can be rewritten as a linear-time computation.

Our fisheye dataset is extremely sparse due to the nature of LIDAR sensors, the loss function is adapted to this sparsity. By masking out pixels that do not have a valid depth value, the loss is calculated only on pixels which have depth values. This facilitates efficient feature extraction by the neural network. In addition to the scale-invariant error, we evaluate our method using the error metrics used in [2,3] as described in section 4.

### 3.3 Training-Model

We train our model in a single pass in an end-to-end fashion compared to [1,2] where the first two scales of the network were trained jointly. For each gradient step, the entire image area is considered for training. Pre-trained weights from AlexNet [13] are used. ConvNet is incorporated as a fixed feature extractor for our dataset and the last fully-connected layers are removed. The fully connected layers are initialized randomly with values from a normal truncated distribution. Scale 2 and Scale 3 are randomly initialized. The dataset contains 55 000 images from fisheye camera and sparse Velodyne HDL-64L rotating 3D laser scanner as ground truth with validation and test set of 1000 and 5000 images respectively. We trained our model with a batch size of 20 using the



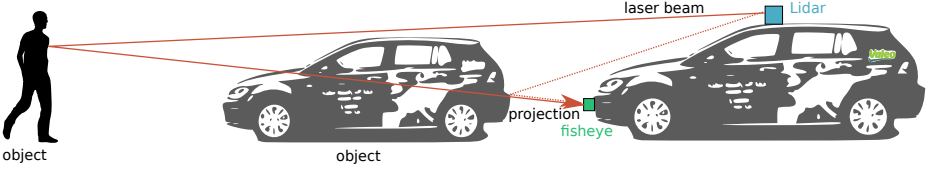


**Fig. 3.** Illustration of occlusion due to LIDAR’s viewpoint being higher than the fisheye camera’s viewpoint. 3D points from the object (person) will be mapped to image plane even though it is not visible from camera.

Adam [34] optimization algorithm, with  $\beta_1 = 0.9$ ,  $\beta_2 = 0.999$  and  $\epsilon = 10^{-8}$ . We adopt an exponential decay function to lower the learning rate as the training progresses, with an initial learning rate of  $\lambda = 10^{-4}$ . The function decays every 7500 steps with a base of 0.95. For the non-linearities in the network, we used swish [32] activation function instead of the commonly used rectified linear units (ReLU) [33] which tend to work better on deeper models. The swish function is given by [32]:

$$f(x) = x \cdot \sigma(x), \quad (5)$$

where  $\sigma(x) = (1 + e^{-x})^{-1}$  is the sigmoid function. The interesting aspect about the swish is that it does not monotonically increase compared to other activations functions. ReLU is defined by  $f(x) = \max(0, x)$ , a major drawback is that for half the values of the input  $x$  its derivative is 0. The problem of *dead neurons* arises as the parameter will not be updated if the gradient is 0, since gradient descent being the parameter update algorithm. We initially experimented by adopting different proposed alternative activation functions such as SELU [35], ELU [36] and leaky ReLU [37]. However, we found that swish performed better. The advantage of using swish as an activation function is that it can be re-parameterized in order to *stretch out* the sigmoid:

$$f(x) = 2 \cdot x \cdot \sigma(\beta \cdot x), \quad (6)$$

In equation 6 if  $\beta = 0$ ,  $f$  becomes the identity activation and if  $\beta \rightarrow \infty$  the sigmoid converges to the unit step and multiplying that by  $x$  gives back  $f(x) = 2 \cdot \max(0, x)$  nothing but ReLU multiplied by a constant factor. Hence, the inclusion of  $\beta$  nonlinearly interpolates between identity and ReLU [38].

### 3.4 Occlusion Correction

The sensor fusion of the data will be correct, if both camera and the Velodyne LIDAR scanner beholds the world from the same viewpoint. However, in our vehicle, the fisheye cameras are in the front and LIDAR is placed at the top as seen in Fig. 3. LIDAR perceives the environment behind objects that occlude the view for the camera. This problem of occlusion results in wrong mapping of depth-points that are not visible to the camera. It is hard to solve, since occluded points are projected adjacently to unoccluded points.

To solve this problem, we adapted a distance based segmentation technique with morphological filters as shown in the Fig. 4. Instead of directly projecting points from

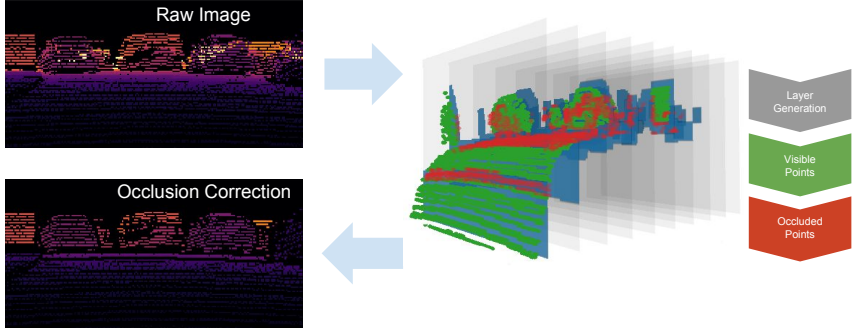


**Fig. 4.** Visualization of the distance based segmentation technique with morphological filters. LIDAR points are projected to corresponding layers and are removed if they are occluded by dilated parts of a neighboring layer.

the LIDAR into the image plane of the fisheye camera, we introduce  $I$  layers within the camera view located at a distance  $d_i^{\text{img}}$ ,  $i = 1, \dots, I$ . Each LIDAR point will be projected onto the layer next to it. We apply a morphological filter that dilates points within each layer to fill the sparse regions (in Fig. 4 dilated parts of the layers are colored blue). A point at a distance  $d$  is regarded as occluded, if a layer  $i$  exists with  $d_i^{\text{img}} < d$ . Otherwise the valid point is projected onto the image plane of the fisheye camera.

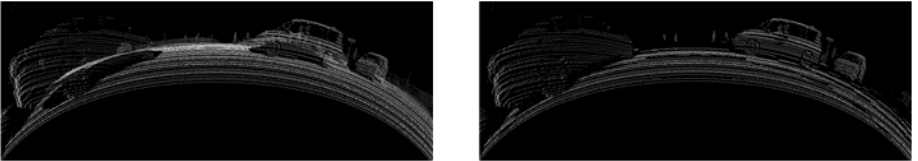


**Fig. 5.** Illustration of Ocluded Velodyne Ground Truth (left) and Dis-Ocluded Velodyne Ground Truth (right)

## 4 Results

The model is completely trained on our internal dataset. Our dataset contains hundred thousand images obtained from raw fisheye camera and sparse Velodyne HDL-64E rotating 3D laser scanner as ground truth. Points without depth value are left unfilled without any post-processing. Eigen’s model [1] handles missing values by eliminating them in the loss function. A ROI of  $1100 \text{ px} \times 330 \text{ px}$  is cropped from the original resolution of  $1280 \text{ px} \times 800 \text{ px}$  to eliminate the upper and lower boundaries with no

depth values and obstruction in the field of view caused by the mounting positions of the fisheye cameras. The cropped images are down-sampled by half to  $576 \text{ px} \times 172 \text{ px}$  primarily to get faster inference and training times.

The ground truth depth for this dataset is captured at various intervals using a Velodyne HDL-64E rotating 3D laser scanner, and are sampled at irregularly spaced points. Conflicting values are found when constructing the ground truth depths for training, since sensor records data at a set maximum frequency of 10 Hz and the fisheye cameras record data at 30 Hz. Time synchronization is essential as the sensors capture data at different frequencies. Each spin of the LIDAR sensor is considered as a frame and carries a time-stamp associated with it. Similarly, each image frame recorded by the fisheye camera carries a time-stamp. For the purpose of synchronization, time-stamps provided with the recordings are used. We resolve conflicts by choosing the depth recorded closest to the RGB capture time in Intempora RTMaps (Real-Time Multisensor Applications) framework.

The training set contains 50 000 images out of 55 000 images collected by driving around Paris, France and various parts of Bavaria, Germany. The remaining 5000 images are used for testing. The training set includes scenes from the *city*, *residential* and *sub-urban* categories of our raw dataset. These are randomly shuffled and fed to the network. We train the entire model for 80 epochs and test prediction takes 3.45 s/batch with a batch size of 20 images (0.17 s/image).

The evaluation of accuracy in our method in depth prediction is using the 3D laser ground truth on the test images. We use the depth evaluation metrics used by Eigen et al. [2].

A protocol evaluation is applied and results are shown by discarding ground-truth depth below 0 m and above 50 m while capping the predicted depths into 0 m – 50 m depth interval. This implies, we set predicted depths to 0 m and 50 m if they are below 0 m or above 50 m, respectively.

In Table 4, we show how our semi-supervised approach performs on Valeo’s fisheye dataset. Furthermore the results of leaderboard algorithms on KITTI 2015 [4] are reproduced. For lack of a better comparison, we use this as a proxy to illustrate that we obtained comparable RMSE on our sparse fisheye dataset. It should be noted that although we predict a dense depth map, the sparse dataset only allows us to take a fraction of the predicted values into consideration for error calculation. To tackle this problem we plan to refine our model on a synthetic dataset, close to our Valeo’s fisheye dataset, that allows a full verification of the predicted depth. First tests show promising results with excluded sky.

## 5 Conclusion

We have demonstrated that semi-supervision using sparse LIDAR data projected on an image plane can be used to reliably produce dense depth estimations for fisheye cameras. To achieve this, we built our own dataset using a 64-beam Velodyne LIDAR and four wide angle fisheye cameras mounted on a self-driving car. As far as the authors are aware, this is the first attempt at CNN based depth estimation on fisheye images using sparse Velodyne ground truth. Even though the camera/LIDAR setups are different, the

**Table 4.** Quantitative results of leaderboard algorithms on KITTI 2015 [4] dataset and our semi-supervised approach on Valeo’s fisheye dataset

Approach	Supervised cap		RMSE	RMSE (log)	ARD	SRD	$\delta < 1.25$	$\delta < 1.25^2$	$\delta < 1.25^3$
			lower is better				higher is better		
Mancini et al. [39]	Yes	0 – 100 m	7.508	0.524	0.196	-	0.318	0.617	0.813
Eigen et al. [2] coarse 28×144	Yes	0 – 80 m	7.216	0.273	0.194	1.531	0.679	0.897	0.967
Eigen et al. [2] fine 27×142	Yes	0 – 80 m	7.156	0.270	0.190	1.515	0.692	0.899	0.967
Liu et al. [40] DCNF-FCSP FT	Yes	0 – 80 m	6.986	0.289	0.217	1.841	0.647	0.882	0.961
Ma et al. [41]	Yes	0 – 100 m	6.266	-	0.208	-	0.591	0.900	0.962
Kuznetsov et al. [5]	No	0 – 50 m	6.182	0.338	0.262	4.537	0.768	0.912	0.955
Zhou et al. [42] (w/o explainability)	No	0 – 50 m	5.452	0.273	0.208	1.551	0.695	0.900	0.964
Garg et al. [43] L12 Aug 8x	No	1 – 50 m	5.104	0.273	0.169	1.080	0.740	0.904	0.962
Zhou et al. [42]	No	0 – 50 m	5.181	0.264	0.201	1.391	0.696	0.900	0.966
Godard et al. [7]	No	0 – 50 m	4.471	0.232	0.140	0.976	0.818	0.931	0.969
Kuznetsov et al. [5]	Yes	0 – 50 m	3.531	0.183	0.117	0.597	0.861	0.964	0.989
Ours fine 80×284	Yes	0 – 50 m	1.717	0.236	0.160	0.397	0.816	0.934	0.969

results provide a reasonable comparison to KITTI on performance of monocular depth regression using sparse LIDAR input. In future work, we aim to improve the results by using more consecutive frames which can exploit the motion parallax and better CNN encoders. We also plan to augment the semi-supervised training with synthetic data and unsupervised training techniques.

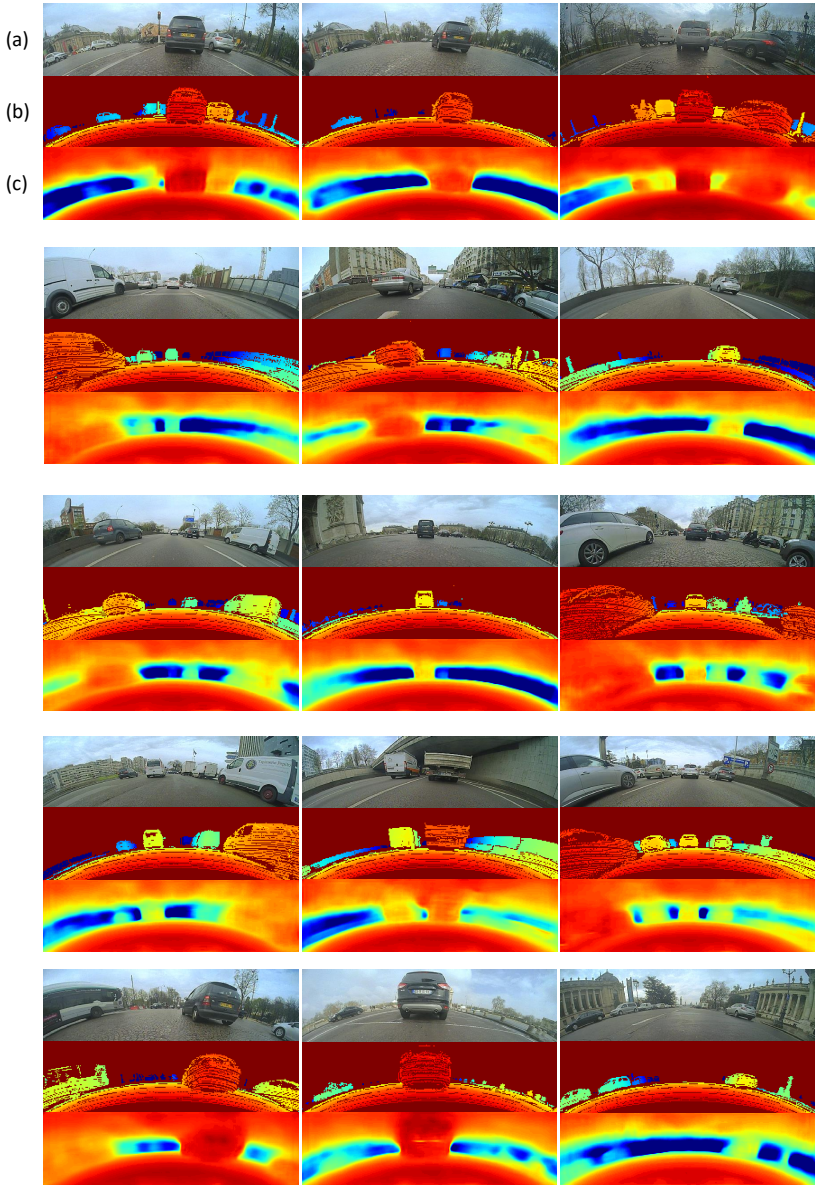


**Fig. 6.** Qualitative results: Example predictions by the proposed CNN network. For each image, we show (a) RGB Input (b) LIDAR Ground Truth (c) Predicted Depth Map<sup>1</sup>

<sup>1</sup> The sky is considered to be invalid pixel i.e masked as zero while training. We have not considered disparity depth for ground truth generation as compared to KITTI [4]. The depth values are in 8-bit intensity range (0 - 255).

## References

1. Eigen, D., Fergus, R.: Predicting depth, surface normals and semantic labels with a common multi-scale convolutional architecture. *CoRR* **abs/1411.4734** (2014)
2. Eigen, D., Puhrsch, C., Fergus, R.: Depth map prediction from a single image using a multi-scale deep network. *CoRR* **abs/1406.2283** (2014)
3. Liu, F., Shen, C., Lin, G., Reid, I.: Learning depth from single monocular images using deep convolutional neural fields. *IEEE Trans. Pattern Anal. Mach. Intell.* **38**(10) (October 2016) 2024–2039
4. Geiger, A.: Are we ready for autonomous driving? the kitti vision benchmark suite. In: *Proceedings of the 2012 IEEE Conference on Computer Vision and Pattern Recognition (CVPR)*. CVPR '12, Washington, DC, USA, IEEE Computer Society (2012) 3354–3361
5. Kuznetsov, Y., Stücker, J., Leibe, B.: Semi-supervised deep learning for monocular depth map prediction. *CoRR* **abs/1702.02706** (2017)
6. Howard, I.P.: Perceiving in depth volume 1 basic mechanisms. (2012)
7. Godard, C., Mac Aodha, O., Brostow, G.J.: Unsupervised monocular depth estimation with left-right consistency. *CoRR* **abs/1609.03677** (2016)
8. Saxena, A., Sun, M., Ng, A.: Make3d: Learning 3d scene structure from a single still image. *IEEE Transactions on Pattern Analysis and Machine Intelligence* **31**(5) (2009) 824840
9. Hoiem, D., Efros, A.A., Hebert, M.: Automatic photo pop-up. *ACM Transactions on Graphics* **24**(3) (Jan 2005) 577
10. Ladický, L., Shi, J., Pollefeys, M.: Pulling things out of perspective. In: *Proceedings of the 2014 IEEE Conference on Computer Vision and Pattern Recognition*. CVPR '14, Washington, DC, USA, IEEE Computer Society (2014) 89–96
11. Karsch, K., Liu, C., Kang, S.B.: In: *Depth Extraction from Video Using Non-parametric Sampling*. Springer Berlin Heidelberg, Berlin, Heidelberg (2012) 775–788
12. Liu, C., Yuen, J., Torralba, A., Sivic, J., Freeman, W.T.: Sift flow: Dense correspondence across different scenes. *Lecture Notes in Computer Science Computer Vision ECCV 2008* (2008) 2842
13. Krizhevsky, A., Sutskever, I., , G.E.: Imagenet classification with deep convolutional neural networks. In Pereira, F., Burges, C.J.C., Bottou, L., Weinberger, K.Q., eds.: *Advances in Neural Information Processing Systems 25*. Curran Associates, Inc. (2012) 1097–1105
14. Girshick, R.B., Donahue, J., Darrell, T., Malik, J.: Rich feature hierarchies for accurate object detection and semantic segmentation. *CoRR* **abs/1311.2524** (2013)
15. Sermanet, P., Eigen, D., Zhang, X., Mathieu, M., Fergus, R., LeCun, Y.: Overfeat: Integrated recognition, localization and detection using convolutional networks. *CoRR* **abs/1312.6229** (2013)
16. Simonyan, K., Zisserman, A.: Very deep convolutional networks for large-scale image recognition. *CoRR* **abs/1409.1556** (2014)
17. Szegedy, C., Liu, W., Jia, Y., Sermanet, P., Reed, S.E., Anguelov, D., Erhan, D., Vanhoucke, V., Rabinovich, A.: Going deeper with convolutions. *CoRR* **abs/1409.4842** (2014)
18. Tompson, J., Jain, A., LeCun, Y., Bregler, C.: Joint training of a convolutional network and a graphical model for human pose estimation. *CoRR* **abs/1406.2984** (2014)
19. Osadchy, M., Cun, Y.L., Miller, M.L.: Synergistic face detection and pose estimation with energy-based models. *Toward Category-Level Object Recognition Lecture Notes in Computer Science* (2006) 196206
20. Zbontar, J., LeCun, Y.: Computing the stereo matching cost with a convolutional neural network. *CoRR* **abs/1409.4326** (2014)

21. Memisevic, R., Conrad, C.: Stereopsis via deep learning. NIPS Workshop on Deep Learning (2011)
22. Gupta, S., Girshick, R.B., Arbelaez, P., Malik, J.: Learning rich features from RGB-D images for object detection and segmentation. CoRR **abs/1407.5736** (2014)
23. Laina, I., Rupprecht, C., Belagiannis, V., Tombari, F., Navab, N.: Deeper depth prediction with fully convolutional residual networks. CoRR **abs/1606.00373** (2016)
24. Karsch, K., Liu, C., Kang, S.B.: Depth extraction from video using non-parametric sampling. Computer Vision ECCV 2012 Lecture Notes in Computer Science (2012) 775788
25. Konrad, J., Wang, M., Ishwar, P.: 2d-to-3d image conversion by learning depth from examples. 2012 IEEE Computer Society Conference on Computer Vision and Pattern Recognition Workshops (2012)
26. Liu, M., Salzmann, M., He, X.: Discrete-continuous depth estimation from a single image. 2014 IEEE Conference on Computer Vision and Pattern Recognition (2014)
27. Liu, B., Gould, S., Koller, D.: Single image depth estimation from predicted semantic labels. 2010 IEEE Computer Society Conference on Computer Vision and Pattern Recognition (2010)
28. Wang, P., Shen, X., Lin, Z., Cohen, S., Price, B., Yuille, A.: Towards unified depth and semantic prediction from a single image. 2015 IEEE Conference on Computer Vision and Pattern Recognition (CVPR) (2015)
29. Li, C., Kowdle, A., Saxena, A., Chen, T.: Toward holistic scene understanding: Feedback enabled cascaded classification models. IEEE Transactions on Pattern Analysis and Machine Intelligence **34**(7) (2012) 13941408
30. Levin, A., Fergus, R., Durand, F., Freeman, W.T.: Image and depth from a conventional camera with a coded aperture. ACM SIGGRAPH 2007 papers on - SIGGRAPH 07 (2007)
31. He, K., Zhang, X., Ren, S., Sun, J.: Deep residual learning for image recognition. CoRR **abs/1512.03385** (2015)
32. Ramachandran, P., Zoph, B., Le, Q.V.: Searching for activation functions. CoRR **abs/1710.05941** (2017)
33. Nair, V., Hinton, G.E.: Rectified linear units improve restricted boltzmann machines. In: Proceedings of the 27th International Conference on International Conference on Machine Learning. ICML'10, USA, Omnipress (2010) 807–814
34. Kingma, D.P., Ba, J.: Adam: A method for stochastic optimization. CoRR **abs/1412.6980** (2014)
35. Klambauer, G., Unterthiner, T., Mayr, A., Hochreiter, S.: Self-normalizing neural networks. CoRR **abs/1706.02515** (2017)
36. Clevert, D., Unterthiner, T., Hochreiter, S.: Fast and accurate deep network learning by exponential linear units (elus). CoRR **abs/1511.07289** (2015)
37. Maas, A.L., Hannun, A.Y., Ng, A.Y.: Rectifier nonlinearities improve neural network acoustic models. In: in ICML Workshop on Deep Learning for Audio, Speech and Language Processing. (2013)
38. Programmer, L.: Deep learning: The swish activation function (Oct 2017)
39. Mancini, M., Costante, G., Valigi, P., Ciarfuglia, T.A.: Fast robust monocular depth estimation for obstacle detection with fully convolutional networks. CoRR **abs/1607.06349** (2016)
40. Liu, F., Shen, C., Lin, G.: Deep convolutional neural fields for depth estimation from a single image. CoRR **abs/1411.6387** (2014)
41. Ma, F., Karaman, S.: Sparse-to-dense: Depth prediction from sparse depth samples and a single image. CoRR **abs/1709.07492** (2017)
42. Zhou, T., Brown, M., Snavely, N., Lowe, D.G.: Unsupervised learning of depth and ego-motion from video. CoRR **abs/1704.07813** (2017)
43. Garg, R., G, V.K.B., Reid, I.D.: Unsupervised CNN for single view depth estimation: Geometry to the rescue. CoRR **abs/1603.04992** (2016)